SUPPLEMENTARY INFORMATION

Sample Description

Rock 14053 is one of the most well-studied high-Al basalts in the Apollo collection [2,3]. This sample (14053,241) was chipped from a large (approx. 0.5 m long) boulder at station C2, about 130 m south of the rim of Cone crater, during EVA 2 of Apollo 14 [4]. Isotopic Rb-Sr studies yielded a well-defined age of 3.92 ±0.04 Ga [5]. This basalt is relatively coarse-grained (0.5-2 mm), typical of other Apollo 14 high-Al basalts, with an ophitic texture, consisting of pyroxene (~50%) and plagioclase (~40%), with the remainder of olivine, ilmenite, chromite-ulvöspinel, silica, in the form of tridymite, FeNi metal, fayalite, troilite, K-Ba-rich glass, K-feldspar, F-Cl apatite, merrillite, and baddeleyite. Clinopyroxenes are strongly zoned in cation abundances and contain Fe-rich rims of ferropyroxene, nearly hedenbergite in composition, but also including pyroxferroite. Typical of most lunar basalts, this rock also contains pockets of late-stage residual "mesostasis", composed of Si- and K-Ba-enriched glass, K-feldspar, fayalite, tridymite, ilmenite, Fe metal, and phosphates. This high-Al basalt formed during assimilation-fractional-crystallization of KREEP by a partial melt from the mantle [6] thereby instilling a higher than normal KREEP signature, largely manifest in the mesostasis. The KREEP component may be responsible for the high H and Cl content observed in these rocks, as KREEP rocks are known to be rich in incompatible elements.

In some of the mesostasis, particularly near the exterior portions of the rock, a unique reduction-breakdown texture of fayalite to Fe metal and silica occurs, indicative of the extreme low fO_2 prevailing during the subsolidus cooling of this rock. This subsolidus reduction of the fayalite is considered to have been imposed upon the 14053 rock after its initial formation, due to incorporation of solar-wind protons and subsequent reheating of the rock in an impact blanket. This hypothesis is consistent with studies on the crystallography of pigeonite in 14053 [7,8], which suggested that this rock originally cooled from an erupted lava, was subsequently re-heated to a temperature higher than 840 $^{\circ}$C, and then cooled rapidly.

Although the apatite in this high-Al basalt is a product of the late-stage crystallization of the residual melt in the mesostasis, it is conceivable that its volatile composition may have been modified by subsequent metasomatism by solar-wind protons. This secondary metamorphism and possible metasomatic effects on the apatite cannot be negated or quantified with the present data.

Analytical Notes

This section contains calibration figures for SIMS analyses of apatite as described in the methods section, as well as a figure detailing the relationship between hydrogen and carbon observed in the apatite and olivine data.

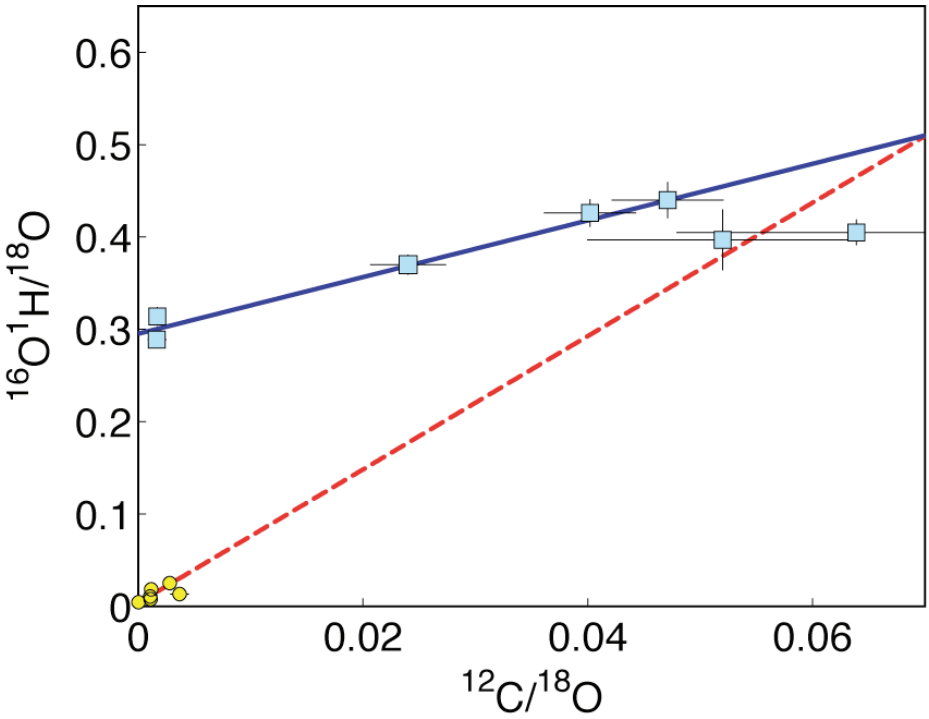

Supplementary Figure 1. Proposed contamination trends for apatite (blue squares) and olivine (yellow circles) in $^{16}O^{1}H/^{18}O$ versus $^{12}C/^{18}O$ space. Error bars are 2σ, visible only where larger than symbol size. Lines represent weighted linear fits to data, dashed where extrapolated.

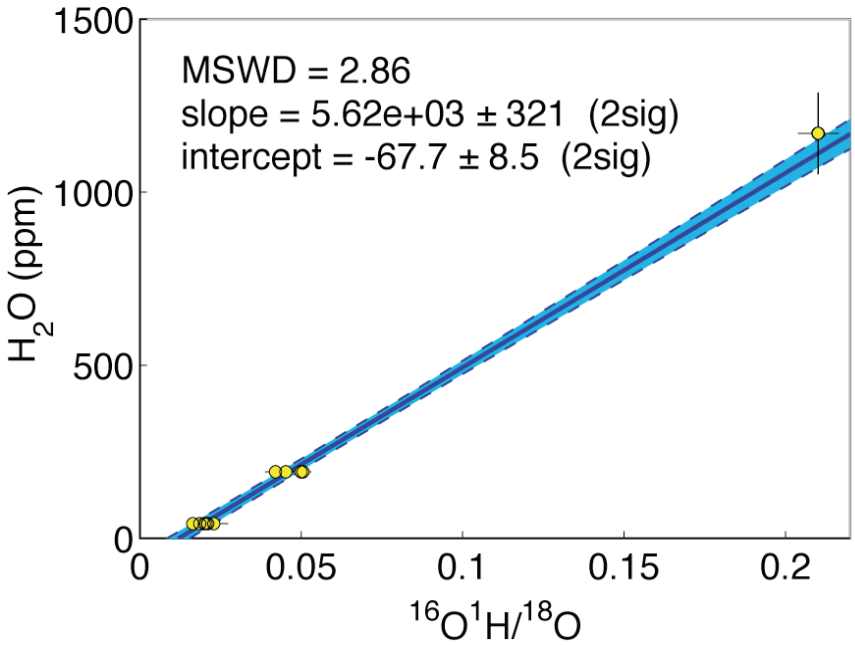

Supplementary Figure 2. Calibration curve for H (reported as H_2O), based on analyses of two synthetic apatites and a well-characterized section of Durango apatite. Uncertainties are 2σ, plotted with 95% confidence bounds. Independent H_2O estimates were determined by FTIR relative to a well-characterized sample of Mud Tank apatite.

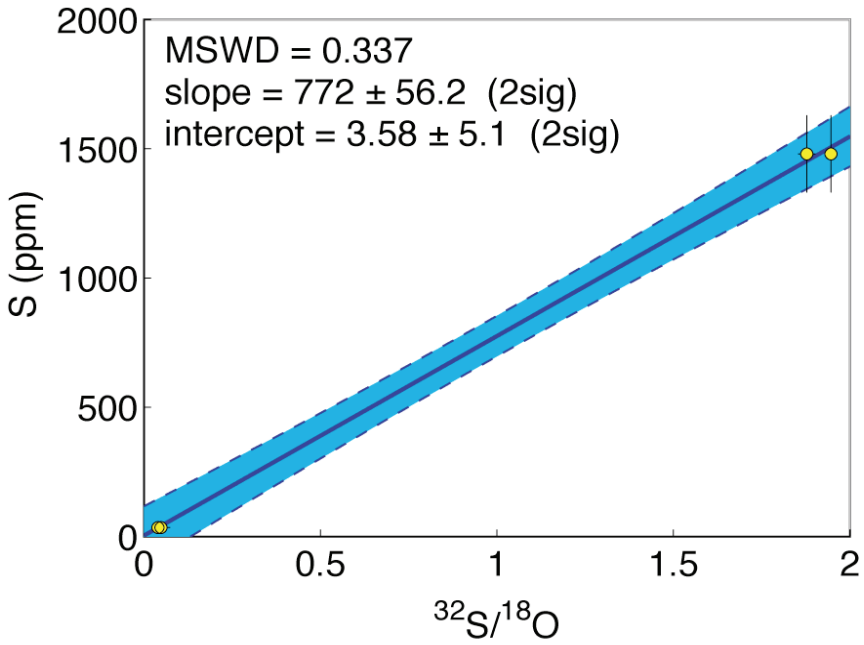

Supplementary Figure 3. Calibration curve for S, based on analyses of Mud Tank and Durango apatite. Uncertainties are 2σ, plotted with 95% confidence bounds. S concentration for Durango from [1]. Mud Tank is a secondary standard with an S concentration of 34.6 ± 2.6 (2σ) ppm, based on >20 previous SIMS analyses. Removing the secondary standard does not significantly change the calibration slope.

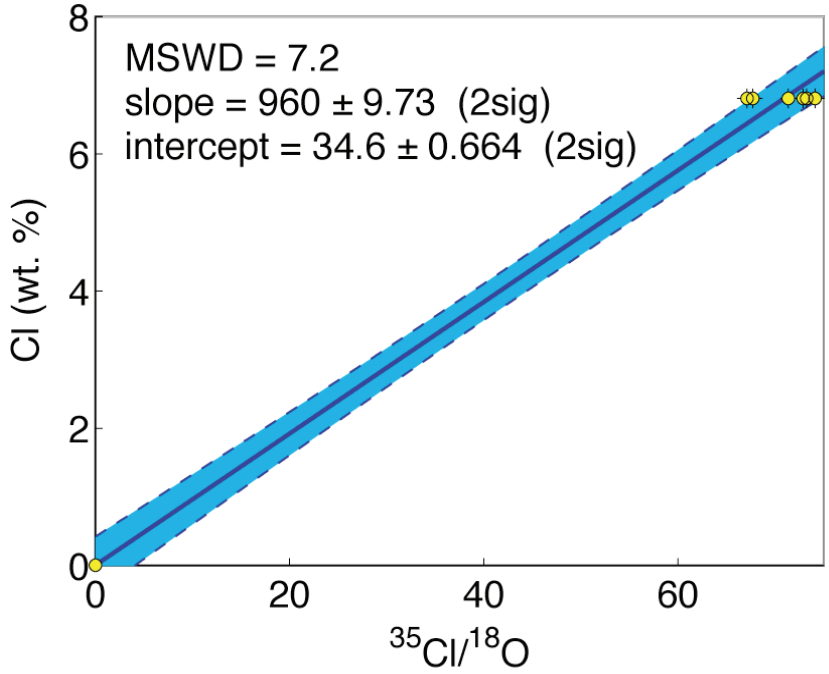

Supplementary Figure 4. Calibration curve for Cl, based on analyses of synthetic chlor- and fluor-apatites. Uncertainties are 2σ, plotted with 95% confidence bounds. Removing the low-Cl secondary standard (synthetic fluorapatite) does not significantly change the calibration slope (which is calculated for Cl as ppm).

Partition Coefficients

In order to relate apatite composition to melt composition, some sort of functional relationship must be developed. In the ideal case, one would make such an estimate based on the solubility product for apatite, considering all of the relevant components and taking into account complications such as the energy of mixing. Such a model requires both thermodynamic and petrologic data that do not exist at the present time. For trace elements, the common practice is to treat the activity coefficients as constants, making the relationship between activity and concentration linear, and therefore, the relationship between concentration in the phases also linear. One must also assume that components such as H and Cl do not change the abundance of apatite, and that substitutions into apatite are independent of each other. Such assertions are likely incorrect in detail, but the magnitude of the effect is unknown. Despite these limitations, this type of treatment has been demonstrated to be robust for apatite-melt equilibrium for both cations Mg[9] and anions Cl [10] over large ranges of concentration. Thus, we expect that for at least Cl, and perhaps for other elements that substitute into the same site (such as H, which enters the apatite structure as OH^-), the constant partition coefficients will provide a reasonable estimate of the volatile content of the

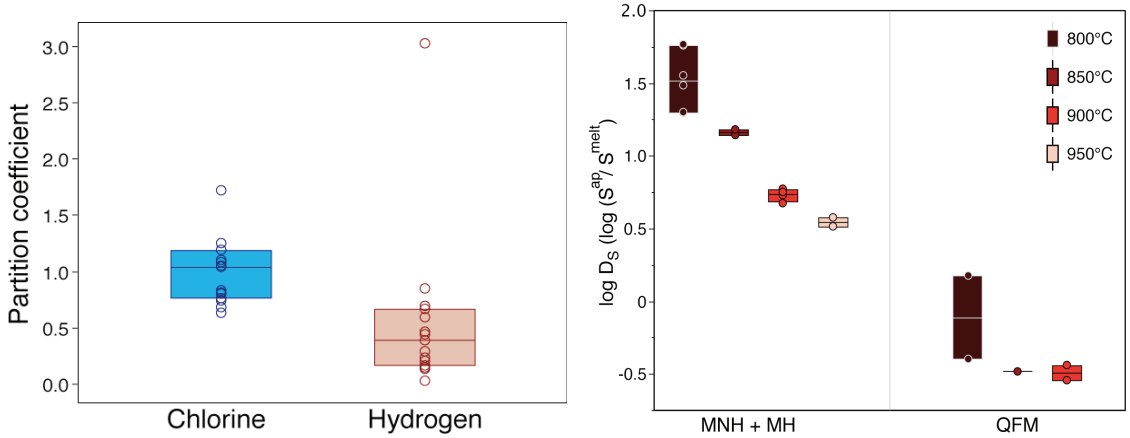

Supplementary Figure 5. Box plots of D_{Cl}, D_H, and D_S, with sulfur plotted as log (D_S) because of large range in values. Log (D_S) is further subdivided as a function of buffer (fO_2 buffered by MH or MNH on left side of diagram, buffered by QFM on right side of diagram) and temperature (color code, increasing temperature to right). Lunar basalts such as 14053 are thought to form under conditions that would plot far off to the right on this diagram in terms of fO_2 (fO_2 << QFM), but at temperatures near the range of these studies (T ~1000°C).

melt in equilibrium with apatite over the range of concentrations observed.

Chlorine partitioning experiments between apatite and mafic melts [10] indicate D_{Cl} values range from ~0.6 to 1.7 (ppm by weight Cl in apatite divided by ppm by weight Cl in melt), with an unweighted mean of 1, while weighted means range from 0.8-0.9, depending on the statistical treatment employed [10]. Using the maximum D_{Cl} would result in a lower estimate of melt Cl concentrations of 800–2000 ppm, whereas the mean D_{Cl} value would give a range of 1300–3500 ppm Cl. The minimum D_{Cl} would suggest that these apatites were in equilibrium with a melt containing more Cl, between 2200 and 5800 ppm. As is the case with all volatile elements, these calculated Cl values might reflect equilibrium with a magma that has already lost Cl relative to F through exsolution of a vapor phase, or via passive, diffusive degassing. Applying the same D_{Cl} methodology to previously published electron probe data on apatite from 14053 yields concentrations of up to 2.6 wt% Cl in the melt [11].

For hydrogen partitioning, we are limited by the lack of direct measurements of H_2O in apatite and coexisting melt. We estimate D_H from observed apatite volatile contents in

experiments [10] where apatite co-exists with H_2O-bearing melts, and the H_2O contents of both phases can be estimated by difference from electron probe totals. These data indicate that D_H values range from 0.13 to 0.85 (with two outliers at higher and lower values, which we omit from our analysis). Taking $D_H = 0.85$ as a maximum yields a minimum H_2O content of 1900 ppm for the melt in equilibrium with apatite in lunar basalt 14053. The mean and minimum values of D_H from those experiments ($D_H = 0.4$ and 0.13) yield 4,000 and 12,000 (1.2 wt. %) ppm H_2O in the melt, respectively. Note that H_2O/F values of melts decrease during degassing, so this apatite may have grown from a melt that had already been depleted in H_2O relative to F.

The existing experimental evidence suggests that sulfur partitioning between apatite and melt is more complicated than for H or Cl [1,12]. The only apatite-melt sulfur partitioning data for mafic melts come from experiments [13] performed at or below 950 °C, and at or above fO_2 in equilibrium with quartz-fayalite-magnetite (QFM) buffer. These experiments demonstrate a strong control of D_S by fO_2 and temperature, with increasing sulfur content in apatite in experiments with high fO_2 and low T (Supplementary Figure 5). The high concentration of sulfur in the lunar apatite is, therefore, unexpected because lunar basalt 14053 is highly reduced. Incorporation of reduced S into the F anion site is known in synthetic apatite [14], but to our knowledge has not been reported in nature. The experimental data are consistent with the incorporation of sulfur into apatite primarily as sulfate, and thus it is reasonable to expect that sulfate availability (controlled in part by fO_2) should strongly influence the amount of sulfur in apatite. Measured S partition coefficients at oxidizing conditions range from 0.29 to 58.5, and vary as a function of T and fO_2 (Supplementary Figure 5). Rock 14053, like all lunar materials, is thought to have formed from a relatively dry magma at high temperatures and low fO_2 (at or below iron-wüstite equilibria, ~5 orders of magnitude lower than QFM, or ΔQFM = -5). Petrologic evidence [11] for an exsolved sulfide liquid in equilibrium with the mesostasis suggests that magma was saturated with sulfur, which for lunar basalts should take place at S concentrations between 1500 and 3400 ppm S [15]. Using these saturation estimates as maximum S contents for the melt allows us to estimate D_S values of 0.14 to 0.31. The fact that this value is not closer to zero suggests that sulfide must also be accommodated into apatite at a finite, non-zero level, because there is very little available sulfate in lunar melts.

1 Peng, G., Luhr, J. F. & McGee, J. J. Factors controlling sulfur concentrations in volcanic apatite. *Am. Mineral.* **82**, 1210-1224 (1997).

2 Neal, C. R., Taylor, L. A. & Patchen, A. D. High alumina (HA) and very high potassium (VHK) basalt clasts from Apollo 14 breccias, Part 1 -- mineralogy and petrology: Evidence of crystallization from evolving magmas. *19th Lunar and Planetary Science Conference*, 137-145 (1989a).

3 Neal, C. R., Taylor, L. A., Schmitt, R. A., Hughes, S. S. & Lindstrom, M. M. High alumina (HA) and very high potassium (VHK) basalt clasts from Apollo 14 breccias, Part 2 -- whole-rock chemistry: Further evidence for combined assimilation and fractional crystallization within the lunar crust. *19th Lunar and Planetary Science Conference*, 147-161 (1989b).

4 Swann, G. A. *et al.* Geology of the Apollo 14 landing site in the Fra Mauro highlands. *USGS Professional Paper* **800**, 103 (1977).

5 Papanastassiou, D. & Wasserburg, G. J. Rb-Sr ages of igneous rocks from the Apollo 14 mission and the age of the Fra Mauro formation. *Earth Planet. Sci. Lett.* **12**, 36-48 (1971).

6 Neal, C. R. & Taylor, L. A. Petrogenesis of mare basalts: A record of lunar evolution. *Geochimica Cosmochimica Acta* **56**, 2177-2211 (1992).

7 Ghose, S., Ng, G. & Walter, L. S. Clinopyroxenes from Apollo 12 and 14: Exsolution, domain structure, and cation order. *3rd Annual Lunar and Planetary Science Conference* **3**, 507-531 (1972).

8 Finger, L. W., Hafner, S. S., Schürmann, K., Virgo, D. & Warburton, D. Distinct Cooling Histories and Reheating of Apollo 14 Rocks. *3rd Annual Lunar and Planetary Science Conference*, 259 (1972).

9 Prowatke, S. & Klemme, S. Trace element partitioning between apatite and silicate melts. *Geochimica Cosmochimica Acta* **70**, 4513-4527 (2006).

10 Mathez, E. & Webster, J. Partitioning behavior of chlorine and fluorine in the system apatite-silicate melt-fluid. *Geochim. Cosmochim. Acta* **69**, 1275-1286, doi:10.1016/j.gca.2004.08.035 (2005).

11 Taylor, L. A., Patchen, A., Mayne, R. G. & Taylor, D.-H. The most reduced rock from the moon, Apollo 14 basalt 14053: Its unique features and their origin. *Am. Mineral.* **89**, 1617 – -1624 (2004).

12 Parat, F. & Holtz, F. Sulfur partitioning between apatite and melt and effect of sulfur on apatite solubility at oxidizing conditions. *Contrib. Mineral. Petrol.* **147**, 201-212 (2004).

13 Luhr, J. F. Experimental Phase Relations of Water- and Sulfur-Saturated Arc Magmas and the 1982 Eruptions of El Chichon Volcano. *J. Petrol.* **31**, 1071-1114 (1990).

14 Henning, P., Adolfsson, E. & Grins, J. The chalcogenide phosphate apatites Ca10(PO4)6S, Sr10(PO4)6S, Ba10(PO4)6S and Ca10(PO4)6Se. *Zeitschrift für Kristallographie* **215**, 226-230 (2000).

15 Wieczorek, M. A. *et al.* The Constitution and Structure of the Lunar Interior. *Reviews in Mineralogy & Geochemistry* **60**, 221-364 (2006).

Table 1 Measured ratios for 14053 apatite, olivine, and standards

Name	$^{12}C/^{18}O$	1σ	$^{16}O^{1}H/^{18}O$	1σ	$^{19}F/^{18}O$	1σ
Lunar_1_1A	1.7E-03	4.2E-04	2.89E-01	4.3E-03	3.0E+01	5.6E+00
Lunar_1_1B	1.7E-03	3.6E-04	3.14E-01	4.9E-03	8.97E+00	6.3E-02
Lunar_1_1C	4.0E-02	2.1E-03	4.26E-01	7.3E-03	8.92E+00	6.7E-02
Lunar_1_1D	2.4E-02	1.7E-03	3.70E-01	5.2E-03	7.10E+01	9.1E-01
Lunar_1_1E	4.7E-02	2.5E-03	4.40E-01	9.6E-03	6.76E+01	6.3E-01
Lunar_1_1F	5.2E-02	6.0E-03	3.97E-01	1.6E-02	6.10E+01	1.7E+00
Lunar_1_1G	6.4E-02	8.0E-03	4.05E-01	6.8E-03	6.14E+01	1.3E+00
Olivine_1_1A	3.7E-03	4.0E-04	1.33E-02	5.4E-04	9.4E-04	2.3E-04
Olivine_1_2A	1.1E-03	1.7E-04	1.1E-02	6.7E-04	7.3E-04	1.7E-04
Olivine_1_2B	2.8E-05	4.3E-05	4.4E-03	4.4E-04	9.3E-04	2.4E-04
Olivine_1_2C	1.2E-03	1.9E-04	1.8E-02	1.2E-03	6.6E-04	1.4E-04
Olivine_1_2D	2.8E-03	2.7E-04	2.51E-02	7.9E-04	1.0E-03	1.5E-04
Olivine_1_3A	1.1E-03	2.3E-04	7.8E-03	5.2E-04	8.9E-04	1.8E-04
Olivine_1_4A	7.6E-03	2.6E-03	9.5E-03	1.0E-03	1.6E-03	3.9E-04
Cl_Ap_A	2.0E-03	6.4E-04	5.3E-02	5.0E-03	2.31E-02	9.4E-04
Cl_Ap_B	1.8E-03	1.4E-04	5.34E-02	9.5E-04	1.83E-02	2.4E-04
Cl_Ap_C	6.9E-04	2.2E-04	3.9E-02	2.1E-03	1.9E-02	1.2E-03
Cl_Ap_D	1.1E-03	4.9E-04	4.9E-02	3.1E-03	2.1E-02	2.9E-03
Cl_Ap_E	4.1E-02	5.5E-03	2.3E-02	2.2E-03	2.0E-02	2.2E-03
Cl_Ap_F	2.4E-04	1.1E-04	1.6E-02	8.7E-04	1.40E-02	6.0E-04
Cl_Ap_G	6.5E-04	1.4E-04	2.11E-02	8.7E-04	1.6E-02	8.2E-04
Cl_Ap_H	1.1E-04	5.5E-05	1.99E-02	8.8E-04	1.5E-02	7.3E-04
Cl_Ap_I	2.4E-04	9.6E-05	2.05E-02	9.3E-04	1.43E-02	6.5E-04
Cl_Ap_J	3.8E-04	1.2E-04	2.0E-02	1.1E-03	1.4E-02	7.2E-04
Dur_A	2.6E-04	7.6E-05	2.10E-01	2.7E-03	7.92E+01	5.5E-01
Dur_B	1.5E-04	7.9E-05	2.10E-01	3.1E-03	7.90E+01	5.8E-01
F_Ap_A	6.1E-04	1.4E-04	5.06E-02	1.2E-03	9.28E+01	6.4E-01
F_Ap_B	2.2E-04	9.5E-05	4.20E-02	1.6E-03	8.98E+01	7.5E-01
F_Ap_C	2.8E-04	1.1E-04	4.99E-02	1.1E-03	8.35E+01	5.0E-01
F_Ap_D	2.1E-04	8.3E-05	4.52E-02	1.3E-03	7.98E+01	3.9E-01
Mud_A	2.50E-02	6.8E-04	2.02E+00	2.2E-02	4.36E+01	9.0E-01
Mud_B	2.42E-02	1.0E-03	2.12E+00	2.1E-02	4.04E+01	8.3E-01

Name	$^{32}S/^{18}O$	1σ	$^{35}Cl/^{18}O$	1σ	$^{16}F^{16}O/^{18}O$	1σ
Lunar_1_1A	4.66E-01	1.5E-02	1.77E+00	2.3E-02	3.42E-01	5.0E-03
Lunar_1_1B	5.96E-01	1.2E-02	3.57E+00	1.8E-02	5.67E-01	8.5E-03
Lunar_1_1C	4.51E-01	6.3E-03	1.63E+00	4.1E-02	5.75E-01	8.5E-03
Lunar_1_1D	4.93E-01	5.8E-03	2.31E+00	2.7E-02	6.12E-01	7.5E-03
Lunar_1_1E	4.79E-01	7.4E-03	2.06E+00	2.7E-02	5.13E-01	6.4E-03
Lunar_1_1F	3.99E-01	7.7E-03	1.36E+00	2.1E-02	3.01E-01	5.8E-03
Lunar_1_1G	4.92E-01	1.2E-02	1.75E+00	1.8E-02	3.87E-01	6.6E-03
Olivine_1_1A	5.1E-04	1.3E-04	7.6E-03	5.7E-04	5.8E-05	4.8E-05
Olivine_1_2A	2.6E-04	1.1E-04	4.7E-03	3.7E-04	-1E-05	5E-08
Olivine_1_2B	1.0E-05	1.5E-05	5.1E-03	7.3E-04	2.2E-05	3.7E-05
Olivine_1_2C	1.9E-04	7.8E-05	5.3E-03	3.6E-04	1.7E-05	2.6E-05
Olivine_1_2D	3.8E-04	8.3E-05	5.5E-03	3.7E-04	1.5E-05	2.3E-05
Olivine_1_3A	1.7E-04	7.9E-05	3.4E-03	3.8E-04	2.0E-05	3.1E-05
Olivine_1_4A	5.9E-03	3.7E-03	5.4E-03	5.9E-04	2.1E-05	3.3E-05
Cl_Ap_A	5.7E-03	1.3E-03	9.17E+01	7.0E-01	2.7E-04	8.5E-05
Cl_Ap_B	3.55E-03	1.1E-04	8.87E+01	8.7E-02	5.8E-04	6.4E-05
Cl_Ap_C	3.0E-03	4.4E-04	9.20E+01	6.2E-01	6.8E-04	1.9E-04
Cl_Ap_D	2.1E-03	8.2E-04	9.55E+01	1.1E+00	8.8E-04	4.4E-04
Cl_Ap_E	5.8E-03	1.3E-03	7.41E+01	1.0E+00	1.1E-04	1.2E-04
Cl_Ap_F	2.1E-03	2.6E-04	6.77E+01	4.8E-01	2.7E-04	9.5E-05
Cl_Ap_G	2.1E-03	2.6E-04	7.29E+01	4.9E-01	2.2E-04	8.7E-05
Cl_Ap_H	1.7E-03	2.6E-04	7.32E+01	4.0E-01	4.9E-05	4.1E-05
Cl_Ap_I	2.2E-03	1.8E-04	7.14E+01	4.0E-01	1.8E-04	6.6E-05
Cl_Ap_J	2.0E-03	2.3E-04	6.71E+01	5.0E-01	5.4E-05	6.5E-05
Dur_A	1.88E+00	1.2E-02	3.85E+00	1.9E-02	6.42E-01	5.8E-03
Dur_B	1.95E+00	8.5E-03	4.43E+00	2.1E-02	5.54E-01	6.0E-03
F_Ap_A	5.3E-03	4.7E-04	7.3E-03	4.5E-04	8.36E-01	8.7E-03
F_Ap_B	4.9E-03	4.4E-04	7.8E-03	5.2E-04	7.64E-01	7.2E-03
F_Ap_C	5.4E-03	4.0E-04	7.5E-03	4.8E-04	5.14E-01	4.7E-03
F_Ap_D	6.1E-03	5.0E-04	6.7E-03	6.1E-04	4.73E-01	4.6E-03
Mud_A	3.97E-02	2.0E-03	4.95E-01	5.7E-03	3.58E-01	4.6E-03
Mud_B	4.8E-02	1.2E-02	5.20E-01	9.1E-03	3.12E-01	5.2E-03

Table 1. Data table of measured ratios for 14053 apatite, olivine, and standards. Apatite standards labelled as follows: "ClAp" (synthetic chlorapatite), "FAp" (synthetic fluorapatite), "Dur" (Durango), "Mud" (Mud Tank).

Table S2 Volatile concentrations in 14053 and standard apatite

Name	H2O (ppm)	2σ	S (ppm)	2σ	Cl (ppm)	2σ
Lunar_1_1A	1554	109	363	41	1734	49
Lunar_1_1B	1697	119	463	43	3460	51
Lunar_1_1C	2322	163	352	33	1602	84
Lunar_1_1D	2008	137	384	35	2248	58
Lunar_1_1E	2405	181	374	35	2016	57
Lunar_1_1F	2161	225	312	31	1337	45
Lunar_1_1G	2205	155	384	39	1718	40
Cl_Ap_A	228	53	8	9	68443	1341
Cl_Ap_B	232	24	6	6	66165	815
Cl_Ap_C	152	27	6	7	68604	1242
Cl_Ap_D	207	37	5	9	71215	1852
Cl_Ap_E	61	21	8	9	71160	2046
Cl_Ap_F	24	11	5	6	65016	1127
Cl_Ap_G	51	14	5	6	69982	1180
Cl_Ap_H	44	13	5	7	70330	1046
Cl_Ap_I	48	14	5	6	68520	1030
Cl_Ap_J	44	14	5	6	64443	1165
Dur_A	1112	78	1453	112	3732	54
Dur_B	1113	80	1506	116	4288	60
F_Ap_A	216	25	8	7	42	6
F_Ap_B	168	24	7	7	42	7
F_Ap_C	213	24	8	6	42	6
F_Ap_D	186	24	8	7	41	9
Mud_A	11280	698	34	9	510	14
Mud_B	11864	724	41	26	533	20

Table 2. Data table of calculated volatile contents for 14053 apatite, olivine and standards. Apatite standards labelled as in Table 1.